Impact of anticyclonic eddies on the spatial distribution and emission of non-methane hydrocarbons in the northern South China Sea

Zhen-Fei Liu[1,2], Wen-Zhu Qiao[3], Ze-Yun Yang[1], Feng Xu[1], Gao-Bin Xu[1], Jian Wang[1], Hao Qiao[1], Cheng-Shuai Li[1], Hong-Hai Zhang[1,2]

[1]Frontiers Science Center for Deep Ocean Multispheres and Earth System, Key Laboratory of Marine Chemistry Theory and Technology, Ministry of Education, Ocean University of China, Qingdao 266100, China

[2]Laoshan Laboratory, Qingdao 266237, China

[3]Weihai Institute of Product Quality Standard and Metrology Inspection, Weihai 264209, China

Correspondence to: Jian Wang (wangjian@ouc.edu.cn) and Hong-Hai Zhang (honghaizhang@ouc.edu.cn)

Abstract. Non-methane hydrocarbons (NMHCs) are important trace active gases that exert significant impacts on climate. Ubiquitous mesoscale eddies likely act as a key physical process regulating the marine emission of these gases, yet the underlying mechanisms remain poorly understood. Herein, we characterized the distributions and emissions of eight C_2–C_5 NMHCs in the South China Sea, with emphasis on the impacts of an anticyclonic eddy. Significantly lower NMHC concentrations were observed in surface seawater within the eddy-controlled region (201 ± 101 pmol L^{-1}) relative to the reference sites (433 ± 62.5 pmol L^{-1}) (*t*-test: $t = 5.645$, $p < 0.001$). Downwelling in the anticyclonic eddy core reduced surface nutrient availability, suppressing the biological production and surface concentrations of alkanes and isoprene, whereas lower alkene levels were mainly driven by weakened photochemical production. The sea-to-air fluxes of NMHCs within the eddy were 56% lower than reference sites, which reduce their potential contributions to ozone and secondary organic aerosol by 59% and 60%, respectively. Overall, our findings elucidate the regulatory role of mesoscale eddies in NMHC dynamics, highlighting their critical function in shaping marine trace gas cycling and associated environmental effects.

1 Introduction

Non-methane hydrocarbons (NMHCs) represent a key subgroup of volatile organic compounds (VOCs) that can exert substantial influences on atmospheric reactivity and global climate patterns (Yuan et al., 2018). Atmospheric NMHCs can participate in reactions with hydroxyl radicals (•OH) and significantly contribute to tropospheric ozone (O_3) production (Atkinson, 2000; Tran et al., 2013). In addition, NMHCs act as essential precursors to secondary organic aerosols (SOA) formation that ultimately impact climate forcing and regional air pollution through cloud condensation nuclei generation, thereby modifying radiation budgets and atmospheric quality (Hallquist et al., 2009; Carpenter et al., 2012; Ding et al., 2013; Krechmer et al., 2015; Riva et al., 2016).

NMHCs have diverse sources, which can be categorized as anthropogenic and natural sources. Key anthropogenic contributions arise from activities such as biomass burning, vehicular emissions, and various industrial operations (Song et al., 2018, 2020), while natural sources comprise emissions by terrestrial plants and marine phytoplankton (Luo and Yu, 2010; Messina et al., 2016). As a primary global reservoir of organic carbon, the ocean is an important natural emission source of NMHCs. Phytoplankton production is considered the principal source of marine dissolved isoprene, and phytoplankton can also produce other NMHCs such as ethane, propane, ethene, and propene (McKay et al., 1996; Broadgate et al., 2004; Dani and Loreto, 2017). Additionally, it has been demonstrated that photodegradation of marine dissolved organic matter (DOM) is another important pathway for NMHC generation (Lee and Baker, 1992; Tran et al., 2013). The photochemical production rate of NMHCs was not only related to the concentration of DOM, but also to its activity, light intensity, and radiation wavelength (Ratte et al., 1998). The removal of NMHCs from seawater occurs through three main mechanisms: sea-to-air exchange, microbial degradation, and hydrochemical reactions, with sea-to-air emission identified as the principal removal pathway for oceanic NMHCs (Gist and Lewis, 2006). Global oceanic NMHC fluxes are estimated at 2–50 Tg C yr^{-1} (Tran et al., 2013), exerting substantial impacts on atmospheric chemical processes within the marine boundary layer (MBL). Specifically, once released from the ocean into the atmosphere, NMHCs rapidly react with •OH, thereby influencing the overall oxidizing capacity of the MBL (Elshorbany et al., 2022). Furthermore, in the MBL of remote marine regions, NMHCs play an

important role in the formation of organic aerosol and contribute to the occurrence of new particle formation events (Tripathi et al., 2024).

As a ubiquitous physical process throughout the global ocean, mesoscale eddies critically modulate circulation patterns and dynamical regimes through energy cascades and material transport (McGillicuddy, 2016). It is well recognized that mesoscale eddies significantly influence ocean biogeochemistry (McGillicuddy et al., 1998; Dai et al., 2020; Liu et al., 2020; Zhang et al., 2023; Zhou et al., 2023). Mesoscale eddies are categorized as anticyclonic, cyclonic, or mode-water eddies according to the vertical displacement (subsidence or uplift) of the main and seasonal thermoclines (McGillicuddy et al., 2007). Generally, anticyclonic eddies can enhance water column stratification and limit upward nutrient replenishment, resulting in diminished primary productivity (Shih et al., 2020). Conversely, by driving upwelling and transporting subsurface nutrients to the euphotic zone, cyclonic eddies may enhance primary productivity and reshape phytoplankton community (Zhou et al., 2020; An et al., 2024). Therefore, mesoscale eddies can significantly modulate primary production within the euphotic zone and influence DOM concentrations and their associated carbon export flux (Zhou et al., 2013, 2020; Liang et al., 2025). Given their pronounced impacts on phytoplankton dynamics and DOM cycling, mesoscale eddies are likely key regulators of NMHC spatial distribution patterns and emissions. However, due to constrained observations, the quantitative understanding of these effects remains limited and fragmented, and the relevant mechanisms are unclear.

The South China Sea (SCS) is the largest semi-enclosed marginal sea in the western Pacific Ocean. The Asian monsoon system drives a distinct seasonal wind reversal over the SCS, with prevailing southwesterlies in summer and northeasterlies in winter. Influenced by the monsoon, Kuroshio waters intrude into the SCS through the Luzon Strait, and the invading Kuroshio branch can lead to seasonal shedding of eddy (Jia and Chassignet, 2011). The combined influences of monsoonal forcing, Kuroshio intrusion, and intricate seabed topography (Men et al., 2024) render the SCS an area of intense eddy activity (Lin et al., 2015), establishing it as a key region for investigating mesoscale ocean processes. Statistical analyses based on satellite altimetry data spanning nearly three decades have revealed that approximately 230 mesoscale eddies occur annually in the SCS, with cyclonic eddies (52.2%) slightly outnumbering anticyclonic eddies (47.8%) (Jin et al., 2024). Eddy activity exhibits notable spatial

heterogeneity. Particularly active regions include the area west of the Luzon Strait, and the offshore region east of Vietnam (Wang et al., 2003). Some eddies in these regions are recurrent, appearing at similar locations and during similar months each year, and are classified as persistent strong eddies (Jin et al., 2024). Here, we investigated NMHC spatial distributions and emissions in the northern SCS, and specifically focused on their response to an anticyclonic eddy. By further assessing the contribution of NMHCs to O_3 and SOA production, we evaluate the potential climate effects induced by mesoscale eddies through their modulation of oceanic NMHC fluxes. This work provides new insights into the pivotal function of mesoscale eddies in regulating NMHC biogeochemical cycles.

2 Materials and methods

2.1 Cruise and sampling

The cruise was conducted in the northern SCS on board the R/V "*Dongfanghong 3*" from 21 August to 4 September 2021. The study area and sampling locations are shown in Fig. 1. Seawater samples were collected from 36 stations, including 9 vertical stations along transect C. During the survey period, sea surface height was higher in the southeastern and western areas than that in the central and northern areas. Further analysis incorporating surface geostrophic currents revealed that a relatively regular-shaped anticyclonic eddy (AE) was present in the west of the study area, while the sea level anomaly (SLA) in the southeastern region lacked the typical structural characteristics of an eddy and was therefore not classified as an anticyclonic eddy. The AE was identified and tracked using satellite altimetry data from the Copernicus Marine Environment Monitoring Service (CMEMS), following the closed-contour method (Chelton et al., 2011), which defines an eddy by its outermost closed SLA contour. The eddy formed through a merger event at the end of July, when a closed SLA contour appeared. The AE was tracked continuously until its SLA signature could no longer be distinguished from the background field, yielding a total lifespan of approximately 100 days before its dissipation in early November. According to established eddy stage classifications defined by lifespan, for example, < 1/3, 1/3–2/3, and 2/3–1 for the intensification, mature, and decay stage, respectively (Sweeney et al., 2003; Zhou et al., 2020), AE was sampled at the end of its intensification stage.

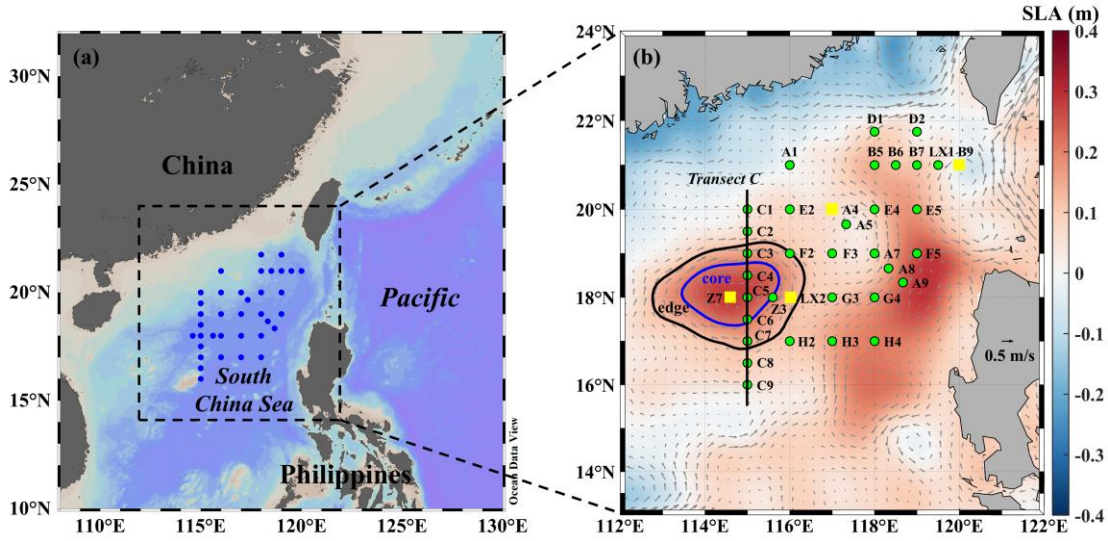

Figure 1. (a) Geographic location of the study area. (b) Locations of sampling stations during the cruise. Yellow squares indicate the stations for photochemical incubation experiments. The background color and vector arrows represent sea level anomaly (SLA, m) and the derived surface geostrophic currents (m s^{-1}) on 21 August 2021, respectively. Transect C that cutting through the core of anticyclonic eddy (AE) was chosen to analyze the sectional distributions of NMHCs. The data for SLA and surface geostrophic current were obtained from Copernicus Marine Service (https://marine.copernicus.eu).

After collection using Niskin bottles (12 L) mounted on a conductivity–temperature–depth (CTD, Sea-Bird 911) rosette, seawater was subsampled into clear glass vials (120 mL). To assess analytical variability, samples were collected in duplicate at 4 stations. To inhibit biological activity, samples were preserved by adding 100 μL of saturated $HgCl_2$ solution. These vials were then sealed without headspace and placed in a dark environment at 4 ℃ for subsequent NMHC determination (Wu et al., 2021, 2023). All samples were delivered to the shore-based laboratory and analyzed within one month. It has been reported that the concentrations of NMHCs in sample vials showed no significant variation over a period of two months (Zhang et al., 2015).

2.2 Analysis of NMHCs

Seawater NMHCs were determined via a purge-and-trap system coupled to a gas chromatography-mass spectrometer (GC-MS, 8860/5977B, Agilent, USA). The target compounds of eight light NMHC species included ethane, propane, i-butane, n-butane, ethene, propene, i-butene, and isoprene. For analysis, a 100 mL sample was purged for 15 min in the extraction chamber by bubbling with pure helium flowing at 80 mL min^{-1}. To eliminate water vapor and carbon dioxide, the gas stream was purified using magnesium perchlorate and sodium hydroxide granules, and subsequently trapped in a liquid nitrogen-

cooled stainless-steel trap. Following thermal desorption with boiling water, the released NMHCs were injected into the GC-MS. Separation and quantification were achieved using the Rt-Alumina BOND/KCl capillary column (30 m × 0.32 mm × 5 μm, Restek, USA). The NMHC standard gas (nominal concentration: 1.00 ppmv in helium, Linde Gas, Germany) was diluted with pure helium to prepare working standards at concentrations of 1, 5, 10, 20, 50, and 100 ppbv. Calibration curves were constructed by plotting the peak area against the concentration of each compound, and linear regression was applied (Fig. S1). The correlation coefficients (R^2) for all target compounds exceeded 0.99. The method detection limits (signal-to-noise ratio of 3) for the eight NMHC species ranged from 0.5 to 1.0 pmol L^{-1}, with precisions (evaluated by analyzing six replicate standards at two concentration levels: 22.3 and 89.3 pmol L^{-1}) between 3% and 6% (see Table S1 for details).

2.3 Analysis of environmental parameters

For Chl-*a* analysis, the seawater samples (1 L) were filtered through GF/F membranes (0.7 μm, Whatman, UK). After folding, membranes were transferred into 15 mL sterilized plastic tubes wrapped in tinfoil, and maintained frozen (−20 ℃) until analysis. Extraction of Chl-*a* was performed by adding 10 mL of 90% (v/v) acetone solution into plastic tubes. After 24 h at 4 ℃, the samples were centrifuged to obtain supernatant, and the fluorescence intensity of the supernatant was determined with a fluorescence spectrophotometer (F-4700, Hitachi, Japan). For dissolved organic carbon (DOC) analysis, the filtrates (30 mL) filtered by GF/F membranes were collected in precombusted (450 ℃ overnight) brown-colored glass vials, and the concentration of DOC was determined with a total organic carbon analyzer (TOC-VCPH, Shimadzu, Japan). For nutrient analysis, the filtrates (50 mL) filtered by GF/F membranes were collected in polyethylene bottles. The concentrations of dissolved inorganic nitrogen (DIN, nitrate + nitrite), silicate, and phosphate were determined with an automatic analyzer (AA3, Seal, Germany). Seawater salinity and temperature were measured using a CTD instrument cluster, while the data on wind speed were recorded by the shipboard meteorological station (AWS430, Vaisala, Finland) installed on the scientific mast at the foremost deck at ~10 m above the sea surface.

2.4 Deck incubation experiments

Seawater sampled from a 5 m depth using Niskin bottles at 4 stations (A4, B9, Z3, and Z7) for NMHC photochemical production rate experiments. To exclude phytoplankton and microbes, seawater was subjected to filtration through polyethersulfone membranes (0.2 μm, PALL, USA). The filtrates were then slowly dispensed into sterile quartz tubes (180 mL, 4 cm in diameter, 15 cm in length) and sealed with screw caps equipped with PTFE-faced silicone septa to ensure no headspace. These quartz tubes were subjected to four distinct optical treatments: (i) unwrapped to receive full-spectrum solar radiation; (ii) wrapped with Mylar-D film to transmit radiation in the visible light (400–700 nm) and ultraviolet A (UVA, 320–400 nm) spectral bands; (iii) wrapped with UF3 Plexiglas to nearly exclusively transmit radiation in visible light spectral bands; and (iv) wrapped with at least three layers of tinfoil to serve as dark controls. For each sampling station, three replicate quartz tubes were prepared for each light treatment. These quartz tubes were subjected to incubation under natural solar radiation in a water bath on the ship's deck. To maintain in situ temperature, the bath was continuously flushed with surface seawater. Incubations were carried out over a 6-hour period (09:00–15:00 local time) to capture the peak intensity of solar radiation. The photochemical production rate was calculated by dividing the increase in NMHC concentration by the incubation time. Furthermore, NMHC photochemical production rates in the visible light, ultraviolet B (UVB, 280–320 nm), and UVA spectral ranges can be estimated by comparing the differences in production rates among the four light-treatment groups. Specifically, the visible light production rate was obtained as (iii) − (iv); the UVA production rate was obtained as (ii) − (iii); the UVB production rate was obtained as (i) − (ii); and the full spectrum production rate was obtained as (i) − (iv). The filtered seawater was assumed to be virus-containing with low microbial biomass, while phytoplankton were effectively removed (Ratte et al., 1993). Given the current lack of clarity and relevant studies regarding the role of viruses in NMHC production and consumption, their potential impact on NMHC dynamics in seawater was not considered in this study. Thus, the measured photochemical production of NMHCs represents net values.

2.5 Calculation of sea-to-air fluxes

The sea-to-air fluxes (F, nmol m^{-2} d^{-1}) of NMHCs were calculated according to Eq. (1):

$$F = k \times (C_w - C_a \times H) \quad (1)$$

where k (m d^{-1}) is the gas transfer velocity; C_w (nmol m^{-3}) is the seawater NMHC concentration; C_a (nmol m^{-3}) is the atmospheric NMHC concentration; and H (dimensionless) is Henry's law constant. Due to the highly supersaturated levels of light NMHCs in surface seawater compared to the atmosphere (exceeding one order of magnitude), atmospheric NMHCs can be considered negligible (Plass-Dülmer et al., 1993); thus, Eq. (1) can be simplified to:

$$F = k \times C_w \quad (2)$$

The gas transfer velocity was calculated following the method of Wanninkhof (2014), as shown in Eq. (3):

$$k = 0.251 \times u^2 \times (S_C/660)^{-0.5} \quad (3)$$

where u (m s^{-1}) is the wind speed at 10 m above the sea level. The Schmidt number S_C is given by the ratio $S_C = \mu / D$, where μ (cm^2 s^{-1}) is the kinematic viscosity of seawater (Wanninkhof, 1992) and D is the diffusion coefficient of the considered species (Wilke and Chang, 1955).

$$\mu = 1.052 + 1.300 \times 10^{-3} \times t + 5.000 \times 10^{-6} \times t^2 - 5.000 \times 10^{-7} \times t^3 \quad (4)$$

$$D = 7.4 \times 10^{-8} \times (q \times M_b)^{0.5} \times T / (n_b \times V_a^{0.6}) \quad (5)$$

where t (°C) is the seawater temperature in Celsius; q is the association factor of water with the value of 2.6; M_b (g mol^{-1}) is the molar weight of water; T (K) is the seawater temperature in Kelvin; n_b is the dynamic viscosity of seawater, and V_a is the molar volume at boiling point.

2.6 Assessment of NMHC environmental effects

A key process governing the chemical transformation of NMHCs in the troposphere is their reaction with •OH. The reactivity of individual NMHCs is quantified by Eq. (6):

$$L_{i,OH} = NMHC_i \times k_{i,OH} \quad (6)$$

where $L_{i,OH}$ (s^{-1}) is the •OH consumption rate of NMHCs; $NMHC_i$ (molecules cm^{-3}) is the concentration of atmospheric NMHCs; and $k_{i,OH}$ (cm^3 $molecule^{-1}$ s^{-1}) is the constant for NMHCs reacting with •OH (Carter, 2010).

NMHC species with greater chemical reactivity are associated with larger contributions to atmospheric O_3 and SOA production (Panda et al., 2015). The role of each NMHC in O_3 and SOA formation was

assessed through the respective calculation of their O_3 formation potential (*OFP*, μg m^{-3}) and SOA formation potential (P_{SOAP}, μg m^{-3}) via Eq. (7) and (8).

$$OFP_i = NMHC_i \times MIR_i \quad (7)$$

$$P_{SOAPi} = NMHC_i \times SOAP_i \times FAC_{toluene} / 100 \quad (8)$$

where $NMHC_i$ (μg m^{-3}) is the concentration of atmospheric NMHCs; MIR_i (g O_3/g VOC) is the maximum O_3 increment reactivity (Carter, 2010); $SOAP_i$ is the tendency (relative to toluene = 100) of each NMHC to form SOA (Derwent et al., 2010); and $FAC_{toluene}$ is the fractional aerosol coefficient of toluene, which has a value of 5.4% (Zhang et al., 2017).

2.7 Statistical analysis

Normality of the data was assessed using the Shapiro-Wilk test, and homogeneity of variances was evaluated using Levene's test. For comparisons between two groups, parametric *t*-tests were applied when both normality and homoscedasticity assumptions were satisfied; otherwise, non-parametric Mann-Whitney *U*-tests were used. For comparisons involving more than two groups, one-way ANOVA was used when assumptions were met, followed by Tukey's post-hoc test for multiple comparisons; otherwise, the Kruskal-Wallis test was employed. For comparisons where sample sizes were too small for meaningful statistical significance testing, Cohen's d was calculated as a measure of effect size to quantify the magnitude of observed differences. A significance threshold of $p < 0.05$ was used in all analyses. Statistical analyses were performed via SPSS 25.

3 Results

3.1 Hydrographic characteristics

Spatial distributions of temperature, salinity, Chl-*a*, and DOC in surface seawater of the northern SCS obtained during the cruise are shown in Fig. 2. The mean (range) of surface temperature and salinity across the survey area were 30.20 ± 0.31 (29.59–30.71) °C and 33.84 ± 0.11 (33.59–34.01), respectively. The high-temperature region corresponded to areas with elevated SLA, with the highest temperatures (30.54 ± 0.12 °C) observed within the AE. Additionally, sea surface salinity was also relatively high within the area controlled by the AE. Based on the SLA and K-means cluster analysis (Tian et al., 2025),

the sampling stations were classified into three categories: eddy core, eddy edge, and reference sites. Detailed SLA values and station classifications were provided in Table S2.

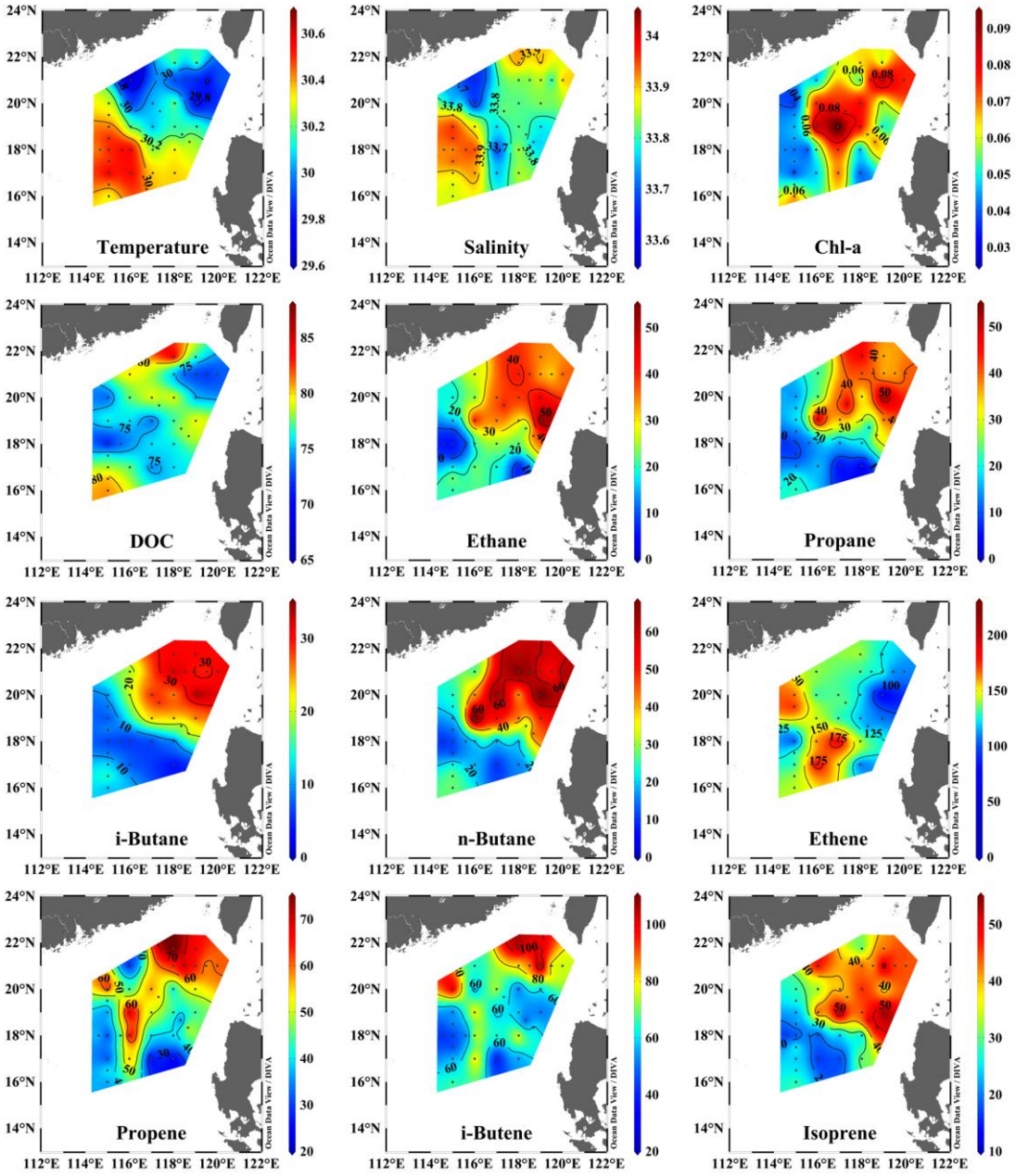

Figure 2. Horizontal distributions of temperature (°C), salinity, Chl-*a* (μg L^{-1}), DOC (μmol L^{-1}), and NMHCs (pmol L^{-1}) in surface seawater of the northern SCS.

The surface Chl-*a* concentration ranged from 0.02 to 0.12 μg L^{-1}, averaging 0.06 ± 0.02 μg L^{-1}, and exhibited clear modulation by the AE. A relatively high Chl-*a* concentration was observed in the northeastern sector of the study area, with an average of 0.07 ± 0.02 μg L^{-1}. In contrast, Chl-*a* concentrations were lowest within the AE, with an average of 0.04 ± 0.01 μg L^{-1}, representing a 39.6% decrease compared to the reference sites (*t*-test: $t = 3.090$, $p = 0.005$). Similarly, the distribution of DOC

was also influenced by the AE, with lower values in the core of AE (72.2 ± 9.6 μmol L^{-1}) and higher concentrations at the reference sites (80.5 ± 8.9 μmol L^{-1}) (Cohen's d = 0.92, large effect size).

3.2 Spatial variability of seawater NMHCs

The concentrations of ethane, propane, i-butane, n-butane, ethene, propene, i-butene, and isoprene in surface seawater ranged from 1.0–64.4, 0.7–67.7, 0.8–49.8, 4.4–99.2, 3.5–239, 21.3–85.0, 32.0–175, and 10.4–64.8 pmol L^{-1}, with mean values of 26.7 ± 15.4, 26.1 ± 17.4, 19.5 ± 13.6, 37.3 ± 25.1, 129 ± 47.1, 48.6 ± 19.3, 69.7 ± 30.3, and 34.1 ± 15.3 pmol L^{-1}, respectively. Alkenes accounted for a relatively large proportion of total NMHCs, with concentrations being 0.9–3.8 times higher than those of alkanes with the same carbon number. The distribution of NMHCs was also significantly influenced by the eddy, with their mean concentrations in the AE-affected area (201 ± 101 pmol L^{-1}) being notably lower than those at the reference sites (433 ± 62.5 pmol L^{-1}) (*t*-test: $t = 5.645$, $p < 0.001$). However, distinct distribution patterns were observed among different species. Alkanes and isoprene exhibited similar horizontal distribution patterns, with elevated values mainly occurring in the central and northeastern regions that were unaffected by the AE. In contrast, the concentrations of alkanes and isoprene in the region controlled by the AE were markedly lower, accounting for only 36.5%–57.9% of the regional average. For C_2–C_4 alkenes, elevated values were observed not only in the northeastern sector but also along the eddy edge. However, their concentrations observed within the eddy core were substantially reduced, representing a 25.5%–37.8% decrease relative to the regional mean. Overall, the mean concentrations of all NMHC components at the AE were significantly reduced relative to the reference sites (*t*-test: $t = 2.132$–5.208, $p < 0.05$; see Table S3).

Transect C crossing through the center of AE shows the vertical profiles of NMHCs (Fig. 3). Within the eddy core, the isolines of alkanes and isoprene displayed a pronounced downward displacement. In the upper 0–50 m layer of the eddy core, their concentrations were markedly depleted compared to the eddy edge and reference sites. Their maximum concentrations were observed below 100 m within the eddy core, whereas at the reference sites, high values generally occurred above 50 m. Unlike alkanes and isoprene, the maximum values of C_2–C_4 alkenes did not exhibit a downward shift at the core of AE.

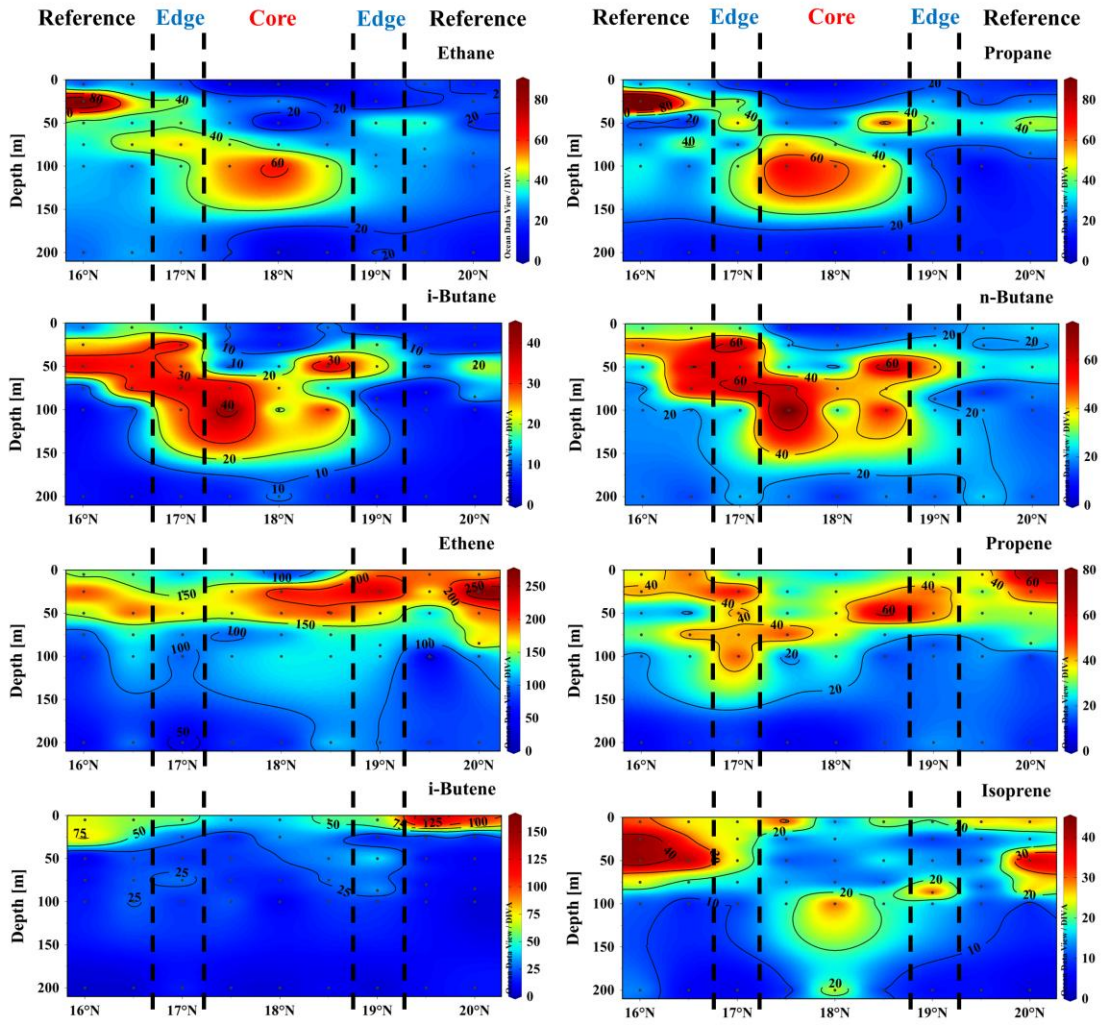

Figure 3. Vertical profiles of NMHCs (pmol L^{-1}) along transect C in the northern SCS.

3.3 Photochemical production rates of NMHCs

Photochemical production was considered an important source of marine NMHCs. In 0.2 μm-filtered seawater, the concentrations of NMHCs increased after 6 hours of solar irradiation (Fig. S2). C_2–C_4 alkenes exhibited the largest enhancement, with increases of 63%–210%, far exceeding the changes observed for other compounds (which increased by 25%–55%). The photochemical production rates of ethane, propane, i-butane, n-butane, ethene, propene, i-butene, and isoprene ranged from 2.5–3.1, 4.3–4.4, 2.4–3.4, 4.0–7.0, 24.1–38.8, 5.3–22.9, 12.2–15.3 and 2.6–4.7 pmol L^{-1} h^{-1}, with mean values of 2.8 ± 0.4, 4.4 ± 0.1, 2.9 ± 0.7, 5.5 ± 2.2, 32.2 ± 6.2, 18.1 ± 8.6, 13.8 ± 1.7, and 3.7 ± 1.5 pmol L^{-1} h^{-1}, respectively (n = 4). Photochemical production rates of C_2–C_4 alkenes were 4–11 times higher than those of alkanes with the same carbon number, indicating that alkenes are the dominant photochemical products (Fig. S2). In addition, the photochemical production rates of C_2–C_4 alkenes showed substantial

spatial variability. The rates of ethene, propene, and i-butene in the eddy core (24.1 ± 2.6, 5.3 ± 0.6, and 12.2 ± 1.2 pmol L^{-1} h^{-1}, respectively; from one station with triplicate incubations) were lower than those at the eddy edge (ethene: 34.6 ± 2.2 pmol L^{-1} h^{-1}; propene: 21.5 ± 1.3 pmol L^{-1} h^{-1}; i-butene: 15.3 ± 0.7 pmol L^{-1} h^{-1}; from one station with triplicate incubations) and at the reference sites (ethene: 35.0 ± 5.4 pmol L^{-1} h^{-1}; propene: 22.8 ± 0.2 pmol L^{-1} h^{-1}; i-butene: 13.9 ± 2.1 pmol L^{-1} h^{-1}; mean ± SD from two stations) (Table 1). Moreover, photochemical production rates differed markedly among individual C_2–C_4 alkenes, and the relative contributions of individual spectral bands varied accordingly. The contributions of different radiation bands to the photochemical production of C_2–C_4 alkenes followed the order UVB > UVA > visible light, with the UVB band accounting for the majority of photochemical production and contributing up to 73.4%.

Table 1. Concentrations of C_2–C_4 alkenes in 0.2 μm-filtered seawater from the northern SCS under dark control and irradiated conditions after 6 hours of solar exposure, and the calculated photochemical production rates (mean ± SD, n = 3).

Category	Station	Species	Concentration (pmol L^{-1})				Photochemical production rate (pmol L^{-1} h^{-1})			
			Dark	Full spectrum	Visible light + UVA	Visible light	Full spectrum	UVB	UVA	Visible light
Eddy core	Z7	Ethene	80.3 ± 1.9	225 ± 14.2	122 ± 8.5	85.1 ± 1.7	24.1 ± 2.6	17.1 ± 1.3	6.1 ± 1.7	0.8 ± 0.2
		Propene	47.9 ± 2.8	79.5 ± 6.5	64.4 ± 3.3	53.2 ± 2.2	5.3 ± 0.6	2.5 ± 0.9	1.9 ± 0.8	0.9 ± 0.4
		i-Butene	37.9 ± 1.4	111 ± 7.9	64.7 ± 4.0	46.9 ± 0.8	12.2 ± 1.2	7.7 ± 0.7	3.0 ± 0.8	1.5 ± 0.3
Eddy edge	LX2	Ethene	108 ± 3.6	315 ± 10.0	163 ± 7.9	120 ± 4.0	34.6 ± 2.2	25.4 ± 2.6	7.1 ± 1.5	2.1 ± 0.6
		Propene	69.0 ± 1.2	198 ± 8.9	120 ± 9.8	82.4 ± 1.9	21.5 ± 1.3	13.0 ± 1.5	6.3 ± 2.0	2.2 ± 0.4
		i-Butene	93.6 ± 4.4	185 ± 7.6	146 ± 8.7	108 ± 4.5	15.3 ± 0.7	6.5 ± 1.4	6.3 ± 0.7	2.5 ± 0.9
Reference site	A4	Ethene	111 ± 4.2	344 ± 14.3	–	–	38.8 ± 3.0	–	–	–
		Propene	83.8 ± 2.3	219 ± 7.5	–	–	22.6 ± 1.5	–	–	–
		i-Butene	80.3 ± 3.6	155 ± 17.9	–	–	12.4 ± 3.0	–	–	–
Reference site	B9	Ethene	91.9 ± 3.5	279 ± 13.0	–	–	31.2 ± 2.6	–	–	–
		Propene	77.0 ± 6.7	215 ± 9.3	–	–	22.9 ± 2.1	–	–	–
		i-Butene	68.8 ± 4.8	161 ± 15.0	–	–	15.3 ± 2.7	–	–	–

"–" indicates that the corresponding experiments were not conducted.

4 Discussion

4.1 Biological controls of alkanes and isoprene under anticyclonic eddy–induced stratification

Anticyclonic eddies are characterized by enhanced upper-ocean stratification and strong water-column convergence, as indicated by the pronounced downward deflections of isotherms and isopycnals in the eddy core (Fig. S3). These physical processes substantially modify the vertical distributions of dissolved nutrients and phytoplankton biomass. Surface nutrients within the AE were very low (DIN: 0.30 ± 0.06 μmol L^{-1}; phosphate: 0.04 ± 0.03 μmol L^{-1}) but increased gradually with depth. Notably, below 75 m, nutrient concentrations in the eddy core (DIN: 5.84 ± 3.55 μmol L^{-1}; phosphate: 0.29 ± 0.22 μmol L^{-1}) were significantly lower than those at the eddy edge (DIN: 11.75 ± 0.35 μmol L^{-1}; phosphate: 0.67 ± 0.13 μmol L^{-1}) and reference sites (DIN: 11.15 ± 1.62 μmol L^{-1}; phosphate: 0.52 ± 0.07 μmol L^{-1}) (ANOVA test, $p < 0.05$), likely reflecting suppressed upward nutrient fluxes under strong convergence in the eddy core. As a consequence of nutrient limitation, the deep chlorophyll maximum (DCM) was displaced downward to ~100 m in the eddy core, markedly deeper than the ~75 m observed at the reference sites and the eddy edge. Moreover, Chl-*a* concentrations within the DCM layer of the eddy core (0.25 ± 0.11 μg L^{-1}) were substantially lower than those at the eddy edge (0.31 ± 0.09 μg L^{-1}) (Cohen's d = 0.55, medium effect size) and reference sites (0.34 ± 0.06 μg L^{-1}) (Cohen's d = 1.08, large effect size). These results indicate that anticyclonic eddy dynamics inhibit phytoplankton growth by enhancing stratification and restricting nutrient supply to the euphotic zone.

Given that phytoplankton are important biological sources of short-chain alkanes and isoprene (McKay et al., 1996; Wang et al., 2023), the suppression of phytoplankton biomass within the AE is expected to reduce the biological production of these NMHCs. This explains the lower surface concentrations of alkanes and isoprene in the core of AE, as well as their pronounced downward displacement in the vertical profiles. This mechanistic interpretation is supported by correlation analysis (Fig. 4). Ethane, propane, i-butane, n-butane, and isoprene were significantly intercorrelated ($r = 0.508$–0.968, $n = 36$, $p < 0.01$) and also showed significant positive correlations with Chl-*a* ($r = 0.403$–0.544, $n = 36$, $p < 0.05$), indicating a common biological control. Overall, anticyclonic eddies declined the nutrient

supply to influence phytoplankton growth, thereby modulating the biological production and spatial distributions of alkanes and isoprene.

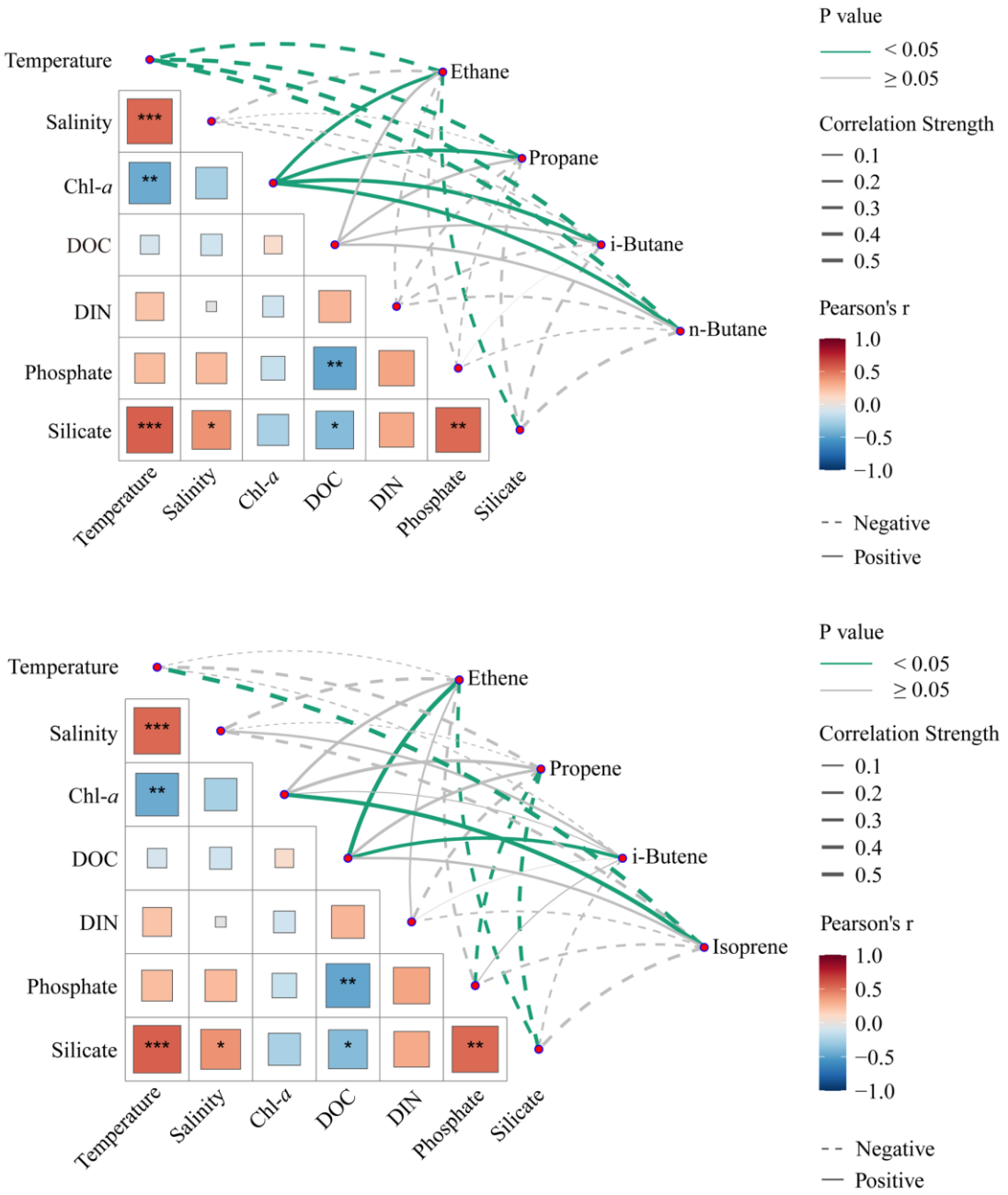

Figure 4. Pearson correlation matrices for environmental parameters and NMHCs in surface seawater, with line thickness and color indicating the strength of the Pearson correlation coefficient (r) and significance (p-value).

It should be noted that the NMHC concentrations represent net values resulting from the balance between biological production and microbial consumption. Previous studies have shown that mesoscale eddies can significantly alter bacterial community structure and activity (Sun et al., 2022; Villegas-Mendoza et al., 2022), thereby influencing the microbial consumption rates of marine reactive gases such

as dimethylsulfide and methane (Li et al., 2025; Wu et al., 2025). Therefore, the eddy-driven variations in bacterial community structure and activity may potentially impact the microbial consumption of NMHCs, and also contribute to the observed spatial patterns of NMHCs.

4.2 Eddy-driven changes in alkene photochemical production and their spectral dependence

The photochemical production rates of C_2–C_4 alkenes varied significantly among stations. However, because the maximum latitudinal extent between the incubation stations was only approximately 330 km, the variations in solar irradiance among stations during the incubation period were minimal (852–895 W m^{-2}), which was insufficient to explain the inter-station differences. Instead, the spatial variability in photochemical production was likely controlled by the availability of photoreactive substrates. Research has indicated that DOC serves as a key substrate for seawater alkenes photoproduction, and its concentrations play an important role in determining alkene production (Ratte et al., 1998). DOC concentrations at the eddy core (Z7: 62.6 μmol L^{-1}) were lower than those at the eddy edge (LX2: 89.8 μmol L^{-1}) and the reference sites (A4: 95.5 μmol L^{-1}; B9: 84.6 μmol L^{-1}). Thus, limited DOC availability within the AE restricted the photochemical formation of C_2–C_4 alkenes, ultimately leading to the lower alkene concentrations inside the eddy. This interpretation is further supported by the significant correlations between DOC and ethene ($r = 0.388$, $n = 36$, $p < 0.05$)/i-butene ($r = 0.505$, $n = 36$, $p < 0.01$). DOC isopleths in vertical profiles showed a downward displacement, with DOC concentrations at 75–100 m in the eddy core markedly higher than those at the eddy edge and reference stations (Fig. S3). However, alkenes showed no comparable distribution pattern, likely due to insufficient light limiting their photochemical production in deeper water.

The relative energy distribution of incident solar radiation across visible light, UVA, and UVB is approximately 90:11:1 (Bird and Riordan, 1986), and this spectral partitioning was used to normalize alkene photochemical production rates to evaluate their wavelength-dependence, with ethene, propene, and i-butene exhibiting UVB:UVA: visible light ratios of 1446:35:1, 707:21:1, and 665:23:1, respectively. Although UVB represents only a small fraction of total solar radiation, its shorter wavelength and higher photon energy are more effective at cleaving photolabile bonds within DOM, resulting in substantially higher photochemical yields of C_2–C_4 alkenes.

We acknowledge that only four photochemical incubation experiments were conducted in this study, which limits the robust assessment of NMHC photoproduction rates between eddy-controlled region and reference stations. Consequently, the observed spectral response patterns and comparisons of photoproduction rates should be considered preliminary. Future investigations with a larger number of incubation experiments are needed to validate these findings. Furthermore, mesoscale eddies can alter the concentration and composition of chromophoric dissolved organic matter (CDOM) through physical processes such as horizontal advection and vertical mixing (Zarokanellos and Jones, 2021; García et al., 2026). Since CDOM is a key substrate for photochemical reactions, eddy-induced variations in CDOM concentrations are expected to influence NMHC photoproduction rates. Therefore, future studies should measure CDOM concentrations to better understand the optical properties of water masses influenced by eddies. Moreover, future research should employ monochromatic irradiation systems to determine wavelength-dependent apparent quantum yields, allowing a more rigorous assessment of spectral dependencies.

4.3 Declined NMHC emissions and associated atmospheric effects within AE

The mean (range) of sea-to-air fluxes of ethane, propane, i-butane, n-butane, ethene, propene, i-butene, and isoprene were 29.4 ± 30.1 (0.8–156), 26.5 ± 33.1 (0.2–184), 18.2 ± 23.1 (0.1–125), 35.0 ± 44.0 (1.2–250), 146 ± 136 (3.0–689), 48.6 ± 45.1 (3.7–225), 60.6 ± 51.7 (8.6–224), and 28.0 ± 24.2 (1.5–132) nmol m^{-2} d^{-1}, respectively. These calculated values were comparable to those reported in the northwestern Pacific Ocean (Li et al., 2019; Wang et al., 2023; Wu et al., 2023), but they were lower than those documented for the Yellow Sea and the East China Sea (Li et al., 2021; Wu et al., 2021; Qiao et al., 2023; Wang et al., 2024) (Table S4). The mean flux of alkenes over the entire study region was 267 ± 240 nmol m^{-2} d^{-1}, approximately 2.5 times higher than that of alkanes (108 ± 128 nmol m^{-2} d^{-1}; Mann-Whitney *U*-tests, $p < 0.001$). In addition, the sea-to-air fluxes of alkenes typically exceed those of alkanes with the same carbon number, corresponding to their respective seawater concentrations.

The seawater NMHC concentration, wind speed, and sea-to-air fluxes of NMHCs at different regions are presented in Fig. 5 (a)–(c). The sea-to-air fluxes of NMHCs were significantly influenced by the AE. Higher fluxes were predominantly observed at the reference sites, in contrast to the lower values within the regions controlled by the AE. Since wind speed showed no significant differences among stations

across different regions, the surface seawater NMHC concentrations were the primary controlling factor that led to the variability of sea-to-air fluxes. Calculations revealed a mean NMHC sea-to-air flux of 196 ± 170 nmol m^{-2} d^{-1} within the AE, representing a 56% reduction relative to the reference sites (447 ± 289 nmol m^{-2} d^{-1}; Mann-Whitney *U*-tests, $p < 0.05$), demonstrating that the anticyclonic eddy suppressed the release of NMHCs.

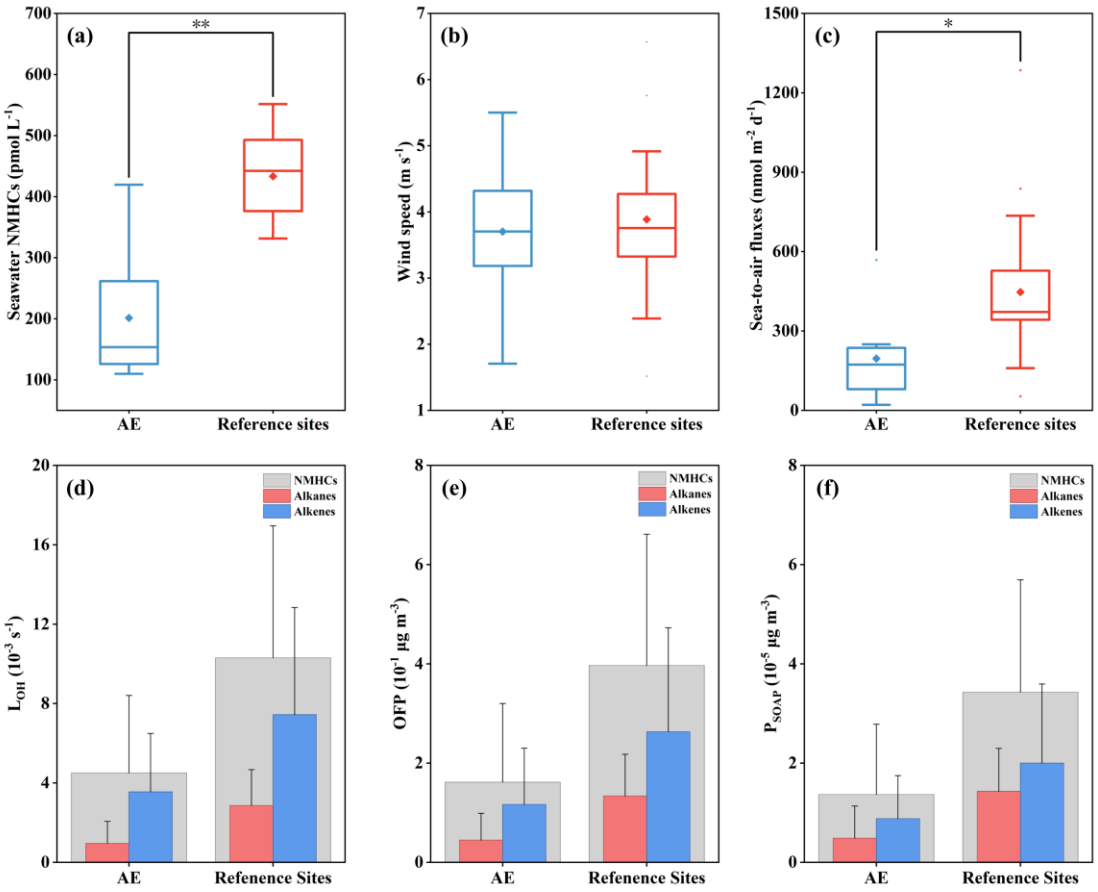

Figure 5. Comparison of NMHC fluxes and associated environmental effects between eddy-influenced regions and reference sites. Box plots show the (a) NMHC concentrations in surface seawater, (b) wind speeds, and (c) sea-to-air fluxes of NMHCs at reference sites and AE-dominated regions. The box boundaries indicate the 25th, 50th (median), and 75th percentiles, respectively, while the mean is denoted by a solid diamond. * and ** indicate statistical significance at the $p < 0.05$ and $p < 0.01$ levels, respectively. Panels d, e, and f show the atmospheric •OH consumption rate, O_3 formation potential, and SOA formation potential of ocean-emitted NMHCs.

To estimate the oceanic contribution to atmospheric NMHCs, we utilized a simple box model with a 500 m boundary layer height (Dacre et al., 2007), with the assumption that the ocean was the sole source of NMHCs. Based on the atmospheric lifetimes (Table 2) and sea-to-air flux of each NMHC, we calculated their resultant atmospheric concentrations attributable to oceanic emissions. The mean atmospheric concentration of NMHCs was 159 ± 166 pptv. Although alkenes exhibited higher sea-to-air

fluxes, alkanes possessed substantially longer atmospheric lifetimes than alkenes, resulting in significantly higher atmospheric alkane concentrations that accounted for up to 90% of the total. Based on the calculated atmospheric NMHC concentrations, we assessed their reactivity in the atmosphere and evaluated their contributions to O_3 and SOA (Table 2).

The mean L_{OH} of ethane, propane, i-butane, n-butane, ethene, propene, i-butene, and isoprene were 0.69 ± 0.71, 0.63 ± 0.79, 0.43 ± 0.54, 0.82 ± 1.03, 3.28 ± 3.06, 1.11 ± 1.03, 1.39 ± 1.19, and 0.64 ± 0.55 (10^{-3} s^{-1}), respectively, with alkenes exhibiting L_{OH} values approximately 2.4 times higher than alkanes. Despite the lower calculated atmospheric concentrations of alkenes relative to alkanes, alkenes exhibited higher L_{OH} values, demonstrating their greater reactivity toward •OH and highlighting their significance as key reactive atmospheric species. To evaluate the relative importance of NMHCs in MBL chemistry, we compared their •OH reactivity with that of dimethylsulfide (DMS), the most abundant biogenic sulfur compound emitted from the ocean. Based on the DMS sea-to-air flux (3.66 ± 4.30 μmol m^{-2} d^{-1}) reported by Wu et al. (2025) for the northern SCS and applying the same atmospheric lifetime approach used for NMHCs, we calculated the average L_{OH} of DMS to be 0.0825 s^{-1}. In comparison, the average L_{OH} of the eight NMHCs measured in this study was 0.00863 s^{-1}, which is approximately 10.5% of the DMS value. The mean *OFP* of NMHCs was 3.30 ± 3.16 (10^{-1} μg m^{-3}), with alkenes contributing the majority, accounting for approximately 64 %. Despite their lower atmospheric concentrations, alkenes generally exhibited higher *OFP* values than alkanes, indicating their crucial role in O_3 formation. However, the P_{SOAP} of alkanes and alkenes were 1.27 ± 1.41 and 1.60 ± 1.54 (10^{-5} μg m^{-3}), respectively, with both groups contributing almost equally to SOA formation.

Within the regions controlled by the AE, the reduced sea-to-air fluxes resulted in lower atmospheric concentrations, leading to diminished L_{OH}, *OFP*, and P_{SOAP} values for both alkanes and alkenes compared to the reference sites (Fig. 5 (d)–(f)). Relative to the reference sites, the O_3 and SOA formation potential of NMHCs at the AE decreased by 59% and 60%, respectively, suggesting that the anticyclonic eddies could substantially weaken the atmospheric environmental impacts of marine NMHCs.

Table 2. Sea-to-air flux, the calculated atmospheric lifetime based on the reaction with •OH, the calculated atmospheric concentrations, •OH consumption rates (L_{OH}), O_3 formation potential (OFP), and SOA formation potential (P_{SOAP}) of each NMHC.

Species	Sea-to-air flux (nmol m^{-2} d^{-1})	Atmospheric lifetime [a] (d)	Calculated concentrations in the atmosphere (pptv)	L_{OH} (10^{-3} s^{-1})	OFP (10^{-1} μg m^{-3})	P_{SOAP} (10^{-5} μg m^{-3})
Ethane	29.4 (0.8–156)	78	101 (1.83–542)	0.69 (0.01–3.70)	0.38 (0.01–2.04)	0.73 (0.01–3.93)
Propane	26.5 (0.2–184)	18	21.2 (0.15–148)	0.63 (0.004–4.42)	0.21 (0.001–1.43)	–
i-Butane	18.2 (0.1–125)	9.1	7.42 (0.03–51.1)	0.43 (0.002–2.94)	0.24 (0.001–1.63)	–
n-Butane	35.0 (1.2–250)	8.2	12.8 (0.45–91.7)	0.82 (0.03–5.86)	0.38 (0.01–2.74)	0.54 (0.02–3.85)
Ethene	146 (3.0–689)	2.3	15.0 (0.24–70.8)	3.28 (0.05–15.51)	1.69 (0.03–7.98)	1.31 (0.02–6.22)
Propene	48.6 (3.7–225)	0.73	1.58 (0.12–7.34)	1.11 (0.08–5.13)	0.35 (0.03–1.61)	0.26 (0.02–1.19)
i-Butene	60.6 (8.6–224)	0.38	1.02 (0.14–3.78)	1.39 (0.20–5.16)	0.16 (0.02–0.60)	0.08 (0.01–0.31)
Isoprene	28.0 (1.5–132)	0.19	0.24 (0.01–1.11)	0.64 (0.03–2.98)	0.08 (0.004–0.36)	0.07 (0.004–0.35)

[a] Assuming a 24-hour average •OH concentration of 6×10^5 molecules cm^{-3} (Jobson et al., 1999) and employing •OH reaction rate constants at 288 K from Atkinson and Arey (2003).

"–" indicates no data.

5 Conclusion

Our study clarifies characteristic NMHC distribution and emission features associated with mesoscale eddies in the northern South China Sea, and further elucidates the mechanisms by which these eddies regulate the production processes of NMHCs. Compared to the reference site, convergence in the surface seawater within the anticyclonic eddy enhanced ocean stratification, which reduced nutrient availability and consequently suppressed phytoplankton growth, leading to decreased concentrations of alkanes and isoprene. For C_2-C_4 alkenes, the reduced photochemical production rates within the anticyclonic eddy served as the key driver for their depressed concentrations in this mesoscale system. Regarding vertical distribution, the peak concentrations of alkanes and isoprene typically occurred at deeper depths with the eddy core. Driven by the anticyclonic eddy, variations in phytoplankton biomass played a key role in shaping the spatial distributions of these NMHCs. In contrast, C_2-C_4 alkenes exhibited no sinking behavior due to the limitation of light radiation. The calculated sea-to-air fluxes indicated that NMHC emissions from the surface seawater of northern SCS made a substantial contribution to the global NMHC inventory. However, the anticyclonic eddy suppressed the emission of NMHCs, reduced the SOA formation potential, and consequently diminished their negative feedback effect on global warming. This study highlights that understanding the mechanisms by which mesoscale dynamical processes influence the distributions and emissions of NMHCs in seawater is essential to assessing the climate-sensitivity of marine NMHC cycling.

Data availability

Data presented in this paper are publicly available on Figshare via https://doi.org/10.6084/m9.figshare.31007650 (Liu, 2026).

Supplement link

The supplement related to this article is available online.

Author contributions

Z-F.L.: Writing–review & editing, Writing–original draft, Investigation, Data curation, Visualization, Conceptualization; W-Z.Q.: Writing–review & editing, Data curation, Conceptualization; Z-Y.Y.: Writing–review & editing; F.X.: Writing–review & editing, Data curation, Conceptualization; G-B.X.: Writing–review & editing; J.W.: Writing–review & editing, Data curation, Conceptualization, Funding acquisition; H.Q.: Writing–review & editing, Conceptualization; C-S.L.: Writing–review & editing; H-H. Z.: Writing–review & editing, Supervision, Resources, Funding acquisition, Conceptualization.

Competing interests

The contact author has declared that none of the authors has any competing interests.

Disclaimer

Publisher's note: Copernicus Publications remains neutral with regard to jurisdictional claims made in the text, published maps, institutional affiliations, or any other geographical representation in this paper. The authors bear the ultimate responsibility for providing appropriate place names. Views expressed in the text are those of the authors and do not necessarily reflect the views of the publisher.

Acknowledgements

We sincerely thank the chief scientist of the open research cruise NORC2021-05 and all crew members of R/V "*Dongfanghong* 3" for their assistance in sampling and providing the CTD data.

Financial support

This work was supported by the National Natural Science Foundation of China (grant numbers 42576041, 42506044, and 42276042), the Laoshan National Laboratory Science and Technology Innovation Program Project (LSKJ202400202 and LSKJ202201701), the Fundamental Research Funds for the Central Universities (202572001 and 842513018), and the General Program of China Postdoctoral Science Foundation (2025M770876).

References

An, L., Liu, X., Xu, F., Fan, X., Wang, P., Yin, W., and Huang, B.: Different responses of plankton community to mesoscale eddies in the western equatorial Pacific Ocean, Deep-Sea Res. Pt. I, 203, 104219, https://doi.org/10.1016/j.dsr.2023.104219, 2024.

Atkinson, R.: Atmospheric chemistry of VOCs and NOx, Atmos. Environ., 34, 2063–2101, https://doi.org/10.1016/S1352-2310(99)00460-4, 2000.

Atkinson, R. and Arey, J.: Atmospheric degradation of volatile organic compounds, Chem. Rev., 103, 4605–4638, https://doi.org/10.1021/cr0206420, 2003.

Bird, R. E. and Riordan, C.: Simple solar spectral model for direct and diffuse irradiance on horizontal and tilted planes at the Earth's surface for cloudless atmospheres, Journal of Climate and Applied Meteorology, 25, 87–97, https://www.jstor.org/stable/26182461, 1986.

Broadgate, W. J., Malin, G., Küpper, F. C., Thompson, A., and Liss, P. S.: Isoprene and other non-methane hydrocarbons from seaweeds: a source of reactive hydrocarbons to the atmosphere, Mar. Chem., 88, 61–73, https://doi.org/10.1016/j.marchem.2004.03.002, 2004.

Carpenter, L. J., Archer, S. D., and Beale, R.: Ocean-atmosphere trace gas exchange, Chem. Soc. Rev., 41, 6473–6506, https://doi.org/10.1039/C2CS35121H, 2012.

Carter, W. P. L.: Development of the SAPRC-07 chemical mechanism, Atmos. Environ., 44, 5324–5335, https://doi.org/10.1016/j.atmosenv.2010.01.026, 2010.

Chelton, D. B., Schlax, M. G., and Samelson, R. M.: Global observations of nonlinear mesoscale eddies, Prog. Oceanogr., 91, 167–216, https://doi.org/10.1016/j.pocean.2011.01.002, 2011.

Dacre, H. F., Gray, S. L., and Belcher, S. E.: A case study of boundary layer ventilation by convection and coastal processes, J. Geophys. Res.-Atmos., 112, D17106, https://doi.org/10.1029/2006JD007984, 2007.

Dai, S., Zhao, Y., Liu, H., Hu, Z., Zheng, S., Zhu, M., Guo, S., and Sun, X.: The effects of a warm-core eddy on chlorophyll *a* distribution and phytoplankton community structure in the northern South China Sea in spring 2017, J. Mar. Syst., 210, 103396, https://doi.org/10.1016/j.jmarsys.2020.103396, 2020.

Dani, K. G. S. and Loreto, F.: Trade-off between dimethyl sulfide and isoprene emissions from marine phytoplankton, Trends Plant Sci., 22, 361–372, https://doi.org/10.1016/j.tplants.2017.01.006, 2017.

508 Derwent, R. G., Jenkin, M. E., Utembe, S. R., Shallcross, D. E., Murrells, T. P., and Passant, N. R.:
509 Secondary organic aerosol formation from a large number of reactive man-made organic compounds,
510 Sci. Total Environ., 408, 3374–3381, https://doi.org/10.1016/j.scitotenv.2010.04.013, 2010.
511 Ding, X., Wang, X., Xie, Z., Zhang, Z., and Sun, L.: Impacts of Siberian biomass burning on organic
512 aerosols over the North Pacific Ocean and the Arctic: primary and secondary organic tracers, Environ.
513 Sci. Technol., 47, 3149–3157, https://doi.org/10.1021/es3037093, 2013.
514 Elshorbany, Y., Zhu, Y., Wang, Y., Zhou, X., Sanderfield, S., Ye, C., Hayden, M., and Peters, A. J.:
515 Seasonal dependency of the atmospheric oxidizing capacity of the marine boundary layer of Bermuda,
516 Atmos. Environ., 289, 119326, https://doi.org/10.1016/j.atmosenv.2022.119326, 2022.
517 García, J. L., Arístegui, J., Pazó, M. J., Vieitez dos Santos, V., Hernández-Hernández, N., Nieto-Cid, M.,
518 Gelado-Caballero, M. D., Martínez-Marrero, A., and Álvarez-Salgado, X. A.: Mesoscale and
519 submesoscale variability of organic matter in island-induced eddies across their life cycle: implications
520 for the biological carbon pump, Front. Mar. Sci., 13, 1711689,
521 https://doi.org/10.3389/fmars.2026.1711689, 2026.
522 Gist, N. and Lewis, A. C.: Seasonal variations of dissolved alkenes in coastal waters, Mar. Chem., 100,
523 1–10, https://doi.org/10.1016/j.marchem.2005.10.004, 2006.
524 Hallquist, M., Wenger, J. C., Baltensperger, U., Rudich, Y., Simpson, D., Claeys, M., Dommen, J.,
525 Donahue, N. M., George, C., Goldstein, A. H., Hamilton, J. F., Herrmann, H., Hoffmann, T., Iinuma,
526 Y., Jang, M., Jenkin, M. E., Jimenez, J. L., Kiendler-Scharr, A., Maenhaut, W., McFiggans, G., Mentel,
527 T. F., Monod, A., Prévôt, A. S. H., Seinfeld, J. H., Surratt, J. D., Szmigielski, R., and Wildt, J.: The
528 formation, properties and impact of secondary organic aerosol: current and emerging issues, Atmos.
529 Chem. Phys., 9, 5155–5236, https://doi.org/10.5194/acp-9-5155-2009, 2009.
530 Jia, Y. and Chassignet, E. P.: Seasonal variation of eddy shedding from the Kuroshio intrusion in the
531 Luzon Strait, J. Oceanogr., 67, 601–611, https://doi.org/10.1007/s10872-011-0060-1, 2011.
532 Jin, Y., Jin, M., Wang, D., and Dong, C.: Statistical analysis of multi-year South China Sea eddies and
533 exploration of eddy classification, Remote Sens., 16, 1818, https://doi.org/10.3390/rs16101818, 2024.
534 Jobson, B. T., McKeen, S. A., Parrish, D. D., Fehsenfeld, F. C., Blake, D. R., Goldstein, A. H., Schauffler,
535 S. M., and Elkins, J. W.: Trace gas mixing ratio variability versus lifetime in the troposphere and

stratosphere: observations, J. Geophys. Res.-Atmos., 104, 16091–16113, https://doi.org/10.1029/1999JD900126, 1999.

Krechmer, J. E., Coggon, M. M., Massoli, P., Nguyen, T. B., Crounse, J. D., Hu, W., Day, D. A., Tyndall, G. S., Henze, D. K., Rivera-Rios, J. C., Nowak, J. B., Kimmel, J. R., Mauldin, R. L. I., Stark, H., Jayne, J. T., Sipilä, M., Junninen, H., St. Clair, J. M., Zhang, X., Feiner, P. A., Zhang, L., Miller, D. O., Brune, W. H., Keutsch, F. N., Wennberg, P. O., Seinfeld, J. H., Worsnop, D. R., Jimenez, J. L., and Canagaratna, M. R.: Formation of low volatility organic compounds and secondary organic aerosol from isoprene hydroxyhydroperoxide Low-NO oxidation, Environ. Sci. Technol., 49, 10330–10339, https://doi.org/10.1021/acs.est.5b02031, 2015.

Lee, R. F. and Baker, J.: Ethylene and ethane production in an estuarine river: formation from the decomposition of polyunsaturated fatty acids, Mar. Chem., 38, 25–36, https://doi.org/10.1016/0304-4203(92)90065-I, 1992.

Li, J. L., Zhai, X., Ma, Z., Zhang, H. H., and Yang, G. P.: Spatial distributions and sea-to-air fluxes of non-methane hydrocarbons in the atmosphere and seawater of the Western Pacific Ocean, Sci. Total Environ., 672, 491–501, https://doi.org/10.1016/j.scitotenv.2019.04.019, 2019.

Li, J. L., Zhai, X., Wu, Y. C., Wang, J., Zhang, H. H., and Yang, G. P.: Emissions and potential controls of light alkenes from the marginal seas of China, Sci. Total Environ., 758, 143655, https://doi.org/10.1016/j.scitotenv.2020.143655, 2021.

Li, X. J., Li, S., Gao, X. X., Li, J. L., Xu, F., Zhou, C., Zhang, H. H., and Zhuang, G. C.: Regulation of mesoscale eddies on oceanic methane production, oxidation, and emissions, Glob. Biogeochem. Cycles, 39, e2025GB008500, https://doi.org/10.1029/2025GB008500, 2025.

Liang, Q., Wang, C., Li, Y., Xie, X., Guo, X., Liu, X., Wang, W., Zhang, Z., and Guo, W.: Kuroshio-derived anticyclonic eddies drive lateral transport and transformation of oceanic dissolved organic matter along the continental slope of South China Sea, J. Geophys. Res.-Oceans, 130, e2024JC021718, https://doi.org/10.1029/2024JC021718, 2025.

Lin, X., Dong, C., Chen, D., Liu, Y., Yang, J., Zou, B., and Guan, Y.: Three-dimensional properties of mesoscale eddies in the South China Sea based on eddy-resolving model output, Deep-Sea Res. Pt. I, 99, 46–64, https://doi.org/10.1016/j.dsr.2015.01.007, 2015.

Liu, H., Zhu, M., Guo, S., Zhao, X., and Sun, X.: Effects of an anticyclonic eddy on the distribution and community structure of zooplankton in the South China Sea northern slope, J. Mar. Syst., 205, 103311, https://doi.org/10.1016/j.jmarsys.2020.103311, 2020.

Liu, Z.: Impact of anticyclonic eddies on the spatial distribution and emission of non-methane hydrocarbons in the northern South China Sea, Figshare [data set], https://doi.org/10.6084/m9.figshare.31007650, 2026.

Luo, G. and Yu, F.: A numerical evaluation of global oceanic emissions of α-pinene and isoprene, Atmos. Chem. Phys., 10, 2007–2015, https://doi.org/10.5194/acp-10-2007-2010, 2010.

McGillicuddy, D. J.: Mechanisms of physical-biological-biogeochemical interaction at the oceanic mesoscale, Annu. Rev. Mar. Sci., 8, 125–159, https://doi.org/10.1146/annurev-marine-010814-015606, 2016.

McGillicuddy, D. J., Robinson, A. R., Siegel, D. A., Jannasch, H. W., Johnson, R., Dickey, T. D., McNeil, J., Michaels, A. F., and Knap, A. H.: Influence of mesoscale eddies on new production in the Sargasso Sea, Nature, 394, 263–266, https://doi.org/10.1038/28367, 1998.

McGillicuddy, D. J., Anderson, L. A., Bates, N. R., Bibby, T., Buesseler, K. O., Carlson, C. A., Davis, C. S., Ewart, C., Falkowski, P. G., Goldthwait, S. A., Hansell, D. A., Jenkins, W. J., Johnson, R., Kosnyrev, V. K., Ledwell, J. R., Li, Q. P., Siegel, D. A., and Steinberg, D. K.: Eddy/wind interactions stimulate extraordinary mid-ocean plankton blooms, Science, 316, 1021–1026, https://doi.org/10.1126/science.1136256, 2007.

McKay, W. A., Turner, M. F., Jones, B. M. R., and Halliwell, C. M.: Emissions of hydrocarbons from marine phytoplankton—some results from controlled laboratory experiments, Atmos. Environ., 30, 2583–2593, https://doi.org/10.1016/1352-2310(95)00433-5, 1996.

Men, G., Wan, X., and Ma, W.: The vertical tilt of mesoscale eddy in the northern South China Sea in a high-resolution numerical simulation, J. Geophys. Res.-Oceans, 129, e2024JC021083, https://doi.org/10.1029/2024JC021083, 2024.

Messina, P., Lathière, J., Sindelarova, K., Vuichard, N., Granier, C., Ghattas, J., Cozic, A., and Hauglustaine, D. A.: Global biogenic volatile organic compound emissions in the ORCHIDEE and

MEGAN models and sensitivity to key parameters, Atmos. Chem. Phys., 16, 14169–14202, https://doi.org/10.5194/acp-16-14169-2016, 2016.

Panda, U., Mahapatra, P. S., and Das, T.: Study of C_2–C_5 non-methane hydrocarbons and their ozone formation potential at Bhubaneswar, an eastern coastal site in India, MAPAN, 30, 195–202, https://doi.org/10.1007/s12647-015-0134-4, 2015.

Plass-Dülmer, C., Khedim, A., Koppmann, R., Johnen, F. J., Rudolph, J., and Kuosa, H.: Emissions of light nonmethane hydrocarbons from the Atlantic into the atmosphere, Glob. Biogeochem. Cycles, 7, 211–228, https://doi.org/10.1029/92GB02361, 1993.

Qiao, W. Z., Wu, Y. C., Wang, P., Wang, J., Zhou, L. M., Li, S. T., and Zhang, H. H.: Distribution characteristics and environmental effects of non-methane hydrocarbons in the East China Sea, Cont. Shelf Res., 261, 105023, https://doi.org/10.1016/j.csr.2023.105023, 2023.

Ratte, M., Plass-Dülmer, C., Koppmann, R., Rudolph, J., and Denga, J.: Production mechanism of C2-C4 hydrocarbons in seawater: field measurements and experiments, Glob. Biogeochem. Cycles, 7, 369–378, https://doi.org/10.1029/93GB00054, 1993.

Ratte, M., Bujok, O., Spitzy, A., and Rudolph, J.: Photochemical alkene formation in seawater from dissolved organic carbon: results from laboratory experiments, J. Geophys. Res.-Atmos., 103, 5707–5717, https://doi.org/10.1029/97JD03473, 1998.

Riva, M., Budisulistiorini, S. H., Zhang, Z., Gold, A., and Surratt, J. D.: Chemical characterization of secondary organic aerosol constituents from isoprene ozonolysis in the presence of acidic aerosol, Atmos. Environ., 130, 5–13, https://doi.org/10.1016/j.atmosenv.2015.06.027, 2016.

Shih, Y. Y., Hung, C. C., Tuo, S., Shao, H. J., Chow, C. H., Muller, F. L. L., and Cai, Y. H.: The impact of eddies on nutrient supply, diatom biomass and carbon export in the northern South China Sea, Front. Earth Sci., 8, 537332, https://doi.org/10.3389/feart.2020.537332, 2020.

Song, J., Zhao, Y., Zhang, Y., Fu, P., Zheng, L., Yuan, Q., Wang, S., Huang, X., Xu, W., Cao, Z., Gromov, S., and Lai, S.: Influence of biomass burning on atmospheric aerosols over the western South China Sea: insights from ions, carbonaceous fractions and stable carbon isotope ratios, Environ. Pollut., 242, 1800–1809, https://doi.org/10.1016/j.envpol.2018.07.088, 2018.

618 Song, J., Zhang, Y., Zhang, Y., Yuan, Q., Zhao, Y., Wang, X., Zou, S., Xu, W., and Lai, S.: A case study
619 on the characterization of non-methane hydrocarbons over the South China Sea: implication of land-
620 sea air exchange, Sci. Total Environ., 717, 134754, https://doi.org/10.1016/j.scitotenv.2019.134754,
621 2020.
622 Sun, F., Xia, X., Simon, M., Wang, Y., Zhao, H., Sun, C., Cheng, H., Wang, Y., Hu, S., Fei, J., and Wu,
623 M.: Anticyclonic eddy driving significant changes in prokaryotic and eukaryotic communities in the
624 South China Sea, Front. Mar. Sci., 9, 773548, https://doi.org/10.3389/fmars.2022.773548, 2022.
625 Sweeney, E. N., McGillicuddy, D. J., and Buesseler, K. O.: Biogeochemical impacts due to mesoscale
626 eddy activity in the Sargasso Sea as measured at the Bermuda Atlantic Time-series Study (BATS),
627 Deep-Sea Res. Pt. II, 50, 3017–3039, https://doi.org/10.1016/j.dsr2.2003.07.008, 2003.
628 Tian, J., Zhang, Y., Jing, H., Ren, H., Mao, H., Zhou, H., Zheng, M., Chen, M., Zhang, R., and Chen, M.:
629 Reshaping of new nitrogen regime by anticyclonic eddies in the northern South China Sea, J. Geophys.
630 Res.-Oceans, 130, e2024JC021684, https://doi.org/10.1029/2024JC021684, 2025.
631 Tran, S., Bonsang, B., Gros, V., Peeken, I., Sarda-Esteve, R., Bernhardt, A., and Belviso, S.: A survey of
632 carbon monoxide and non-methane hydrocarbons in the Arctic Ocean during summer 2010,
633 Biogeosciences, 10, 1909–1935, https://doi.org/10.5194/bg-10-1909-2013, 2013.
634 Tripathi, N., Girach, I. A., Kompalli, S. K., Murari, V., Nair, P. R., Babu, S. S., and Sahu, L. K.: Sources
635 and distribution of light NMHCs in the marine boundary layer of the northern Indian Ocean during
636 winter: implications to aerosol formation, J. Geophys. Res.-Atmos., 129, e2023JD039433,
637 https://doi.org/10.1029/2023JD039433, 2024.
638 Villegas-Mendoza, J., Gómez-Ocampo, E., Velásquez-Aristizábal, J., and Rodríguez-Escobar, D.:
639 Microbial metabolic activity in two basins of the Gulf of Mexico influenced by mesoscale structures,
640 J. Mar. Syst., 234, 103781, https://doi.org/10.1016/j.jmarsys.2022.103781, 2022.
641 Wang, G., Su, J., and Chu, P. C.: Mesoscale eddies in the South China Sea observed with altimeter data,
642 Geophys. Res. Lett., 30, 2121, https://doi.org/10.1029/2003GL018532, 2003.
643 Wang, J., Zhang, H. H., Booge, D., Zhang, Y. Q., Li, X. J., Wu, Y. C., Zhang, J. W., and Chen, Z. H.:
644 Isoprene production and its driving factors in the northwest Pacific Ocean, Glob. Biogeochem. Cycles,
645 37(12), e2023GB007841, https://doi.org/10.1029/2023GB007841, 2023.

Wang, J., Xue, L., Ma, Q., Xu, F., Xu, G., Yan, S., Zhang, J., Li, J., Zhang, H., Zhang, G., and Chen, Z.: The role of oceanic ventilation and terrestrial outflow in atmospheric non-methane hydrocarbons over the Chinese marginal seas, Atmos. Chem. Phys., 24, 8721–8736, https://doi.org/10.5194/acp-24-8721-2024, 2024.

Wanninkhof, R.: Relationship between wind speed and gas exchange over the ocean, J. Geophys. Res.-Oceans, 97, 7373–7382, https://doi.org/10.1029/92JC00188, 1992.

Wanninkhof, R.: Relationship between wind speed and gas exchange over the ocean revisited, Limnol. Oceanogr.: Methods, 12, 351–362, https://doi.org/10.4319/lom.2014.12.351, 2014.

Wilke, C. R. and Chang, P.: Correlation of diffusion coefficients in dilute solutions, AIChE Journal, 1, 264–270, https://doi.org/10.1002/aic.690010222, 1955.

Wu, J. W., Xu, F., Yan, S. B., Xu, G. B., Jiang, Y. C., Li, X. R., Zhai, X., Zhou, L. M., Zhang, H. H., and Chen, Z. H.: Effect of anticyclonic eddies on the production and emission of marine dimethylsulfide in the northern South China Sea, Glob. Planet. Change, 252, 104883, https://doi.org/10.1016/j.gloplacha.2025.104883, 2025.

Wu, Y. C., Li, J. L., Wang, J., Zhuang, G. C., Liu, X. T., Zhang, H. H., and Yang, G. P.: Occurance, emission and environmental effects of non-methane hydrocarbons in the Yellow Sea and the East China Sea, Environ. Pollut., 270, 116305, https://doi.org/10.1016/j.envpol.2020.116305, 2021.

Wu, Y. C., Gao, X. X., Zhang, H. H., Liu, Y. Z., Wang, J., Xu, F., Zhang, G. L., and Chen, Z. H.: Characteristics and emissions of isoprene and other non-methane hydrocarbons in the Northwest Pacific Ocean and responses to atmospheric aerosol deposition, Sci. Total Environ., 876, 162808, https://doi.org/10.1016/j.scitotenv.2023.162808, 2023.

Yuan, Q., Lai, S., Song, J., Ding, X., Zheng, L., Wang, X., Zhao, Y., Zheng, J., Yue, D., Zhong, L., Niu, X., and Zhang, Y.: Seasonal cycles of secondary organic aerosol tracers in rural Guangzhou, Southern China: the importance of atmospheric oxidants, Environ. Pollut., 240, 884–893, https://doi.org/10.1016/j.envpol.2018.05.009, 2018.

Zarokanellos, N. D. and Jones, B. H.: Influences of physical and biogeochemical variability of the central Red Sea during winter, J. Geophys. Res.-Oceans, 126, e2020JC016714, https://doi.org/10.1029/2020JC016714, 2021.

Zhang, H. H., Li, J. L., Yang, G. P., Song, Y. C., and Jin, N.: Purge-trap gas chromatography and mass spectrometric method for analysis of isoprene in natural waters, Chin. J. Anal. Chem., 43, 333–337, https://doi.org/10.1016/S1872-2040(15)60812-X, 2015.

Zhang, W., Zhang, C., Zheng, S., Chen, Y., Zhu, M., and Sun, X.: Distribution of picophytoplankton in the northern slope of the South China Sea under environmental variation induced by a warm eddy, Mar. Pollut. Bull., 194, 115429, https://doi.org/10.1016/j.marpolbul.2023.115429, 2023.

Zhang, Z., Wang, H., Chen, D., Li, Q., Thai, P., Gong, D., Li, Y., Zhang, C., Gu, Y., Zhou, L., Morawska, L., and Wang, B.: Emission characteristics of volatile organic compounds and their secondary organic aerosol formation potentials from a petroleum refinery in Pearl River Delta, China, Sci. Total Environ., 584–585, 1162–1174, https://doi.org/10.1016/j.scitotenv.2017.01.179, 2017.

Zhou, K., Dai, M., Kao, S.-J., Wang, L., Xiu, P., Chai, F., Tian, J., and Liu, Y.: Apparent enhancement of ^{234}Th-based particle export associated with anticyclonic eddies, Earth Planet. Sci. Lett., 381, 198–209, https://doi.org/10.1016/j.epsl.2013.07.039, 2013.

Zhou, K., Dai, M., Xiu, P., Wang, L., Hu, J., and Benitez-Nelson, C. R.: Transient enhancement and decoupling of carbon and opal export in cyclonic eddies, J. Geophys. Res.-Oceans, 125, e2020JC016372, https://doi.org/10.1029/2020JC016372, 2020.

Zhou, K., Xu, Y., Kao, S. J., Xiu, P., Wan, X., Huang, B., Liu, X., Du, C., Sun, J., Sun, Z., and Dai, M.: Changes in nutrient stoichiometry in responding to diatom growth in cyclonic eddies, Geosci. Lett., 10, 12, https://doi.org/10.1186/s40562-023-00269-8, 2023.